Document Title	Monte Carlo modelling of the radiance non-uniformity of the calibration unit integrating sphere
Document Number	VLT-TRE-KMO-146607-004
Issue	1
Date	30th March 2006

	Signature	Date
Prepared by: Alexander Prokhorov, Virial Inc.		
Reviewed by:		
Approved by: Paul Clark		
Released by: Paul Carter		

CHANGE RECORD

Issue	**Date**	**Section affected**	**Change Description**
1	30/3/2006		First release

TABLE OF CONTENTS

1. INTRODUCTION

1.1 Scope

This document contains a report, prepared by Alexander Prokhorov of Virial Inc., which contains the results of Monte Carlo modelling of the radiance non-uniformity at the exit ports of the KMOS calibration unit integrating sphere.

The report concludes that non-uniformity over each port could be within the range 0.05% to 0.1%, meeting the goal for spatial (non-)uniformity specified in the pick-off module requirements [AD2 section 3.2.1.5.2].

However, the report also recommends that these results should be considered preliminary and need to be confirmed after experimental measurement of the BRDF of sintered PTFE. This is already planned, as documented in RD1 section 4.8.2.

1.2 Abbreviations

BRDF	Bi-directional Reflectance Distribution Function
FOV	Field Of View
MRPV	Martonchik-Rahman-Pinty-Verstraete
PTFE	PolyTetraFluoroEthylene

2. DOCUMENTS

The latest version and issue date of each document are contained in the KMOS Configuration Item Data List [AD1].

2.1 Applicable Documents

Ref.	Document Title	Document Number
AD1	KMOS Configuration Item Data List	VLT-LIS-KMO-146604-001
AD2	KMOS Pick-Off Sub-System Requirements Specification	VLT-SPE-KMO-146602-003

2.2 Reference Documents

Ref.	Document Title	Document Number
RD1	KMOS Pick-Off Sub-System Design and Analysis Document	VLT-TRE-KMO-146607-002

In case of any conflict between these documents and the Applicable Documents, the information contained in the Applicable Documents shall take precedence.

{The original report is reproduced here with minor changes to the wording and formatting only}

{Note: the coordinate system used in this report (see Figs 2&3) does not match that of the instrument itself}

Monte Carlo modelling of radiance non-uniformity at the exit ports of the KMOS Calibrating Unit Integrating Sphere

3. OBJECTIVE

This modeling work has three main objectives:

1. To develop an algorithm and computer code to allow the calculation, with the accuracy of several hundredths of a percent, of the radiant flux and angular distribution of radiance within the fields of view of the 'detectors' observing the integrating sphere wall through the output ports.
2. To evaluate the differences between radiant flux and radiance distributions for detectors viewing the sphere wall through the upper and lower output ports.
3. To provide the recommendations for integrating sphere calibrator design improvement (optionally, if computed characteristics turn out to be unsatisfactory)

The principal difficulty with the computer modelling consists of the following. The internal surface of the integrating sphere (a form of sintered PTFE) has very high reflectance in the visual and near-IR spectral range. To obtain the convergence of computational process with the given accuracy, a large number of consecutive reflections of radiation inside the sphere should be modelled. The relatively small size of the area irradiated by the incident beam and the necessity to register the radiance in the given direction or radiant flux in the given small solid angle deepens the complexity of the problem. Moreover, up to date, such computations for integrating sphere were performed for diffuse (Lambertian) [1-3] or specular-diffuse [4-6] reflection models for the sphere internal wall. Sintered PTFE and related materials have reflection very close to Lambertian only in certain ranges of incidence and reflection angles, therefore simple Lambertian approximation could be insufficient and the angular reflection properties of real materials must be considered.

To date, the ray-tracing based Monte Carlo method is the only technique that accommodates the direct simulation of non-Lambertian surfaces. The foundation of this technique is the probabilistic treatment of radiation-matter interactions. This approach allows construction of a stochastic model of the system under consideration and an evaluation of its parameters with a large number of ray tracing implementations. The number of realizations of a stochastic process determines the accuracy of the solutions.

4. GEOMETRICAL MODEL OF THE INTEGRATING SPHERE

For simplicity, we considered the detectors as a point object, eliminated the folding mirror and transformed the detector's FOVs into right-circular cones (see Fig. 1).

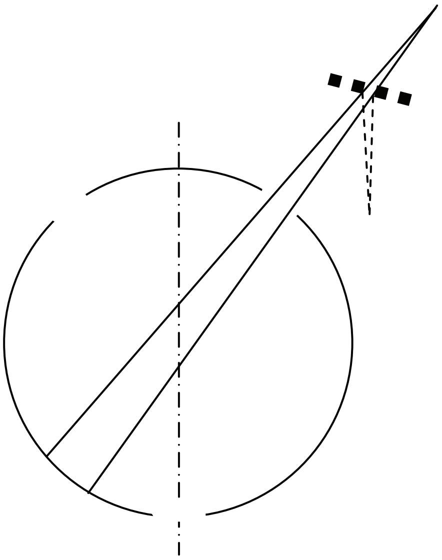

Fig. 1. Elimination of the folding mirror.

The global Cartesian coordinate system, top view and two sections of a geometrical model for the integrating sphere are depicted in Figs. 2-4. We assumed that the sphere has zero thickness (the income of reflection from cylindrical duct of ports is negligible).

If there are N_u upper output port centres and N_l lowers, their angular coordinates are

$$\alpha_{l,i} = \Delta\alpha_l \cdot (i-1); \quad \alpha_{u,k} = \Delta\alpha_u \cdot (k-1) + \frac{\Delta\alpha_l}{2}; \quad i = 1,2,\ldots,N_l; \quad k = 1,2,\ldots,N_u, \tag{1}$$

where $\Delta\alpha_l = 2\pi / N_l; \quad \Delta\alpha_u = 2\pi / N_u$.

Due to the quasi-symmetry of the modelled system about its *z* axis, it is sufficient to investigate one arbitrary port from the upper row and one from the lower row. We will consider the ports corresponding to $i = 1$ and $k = 1$ in Eq. 1.

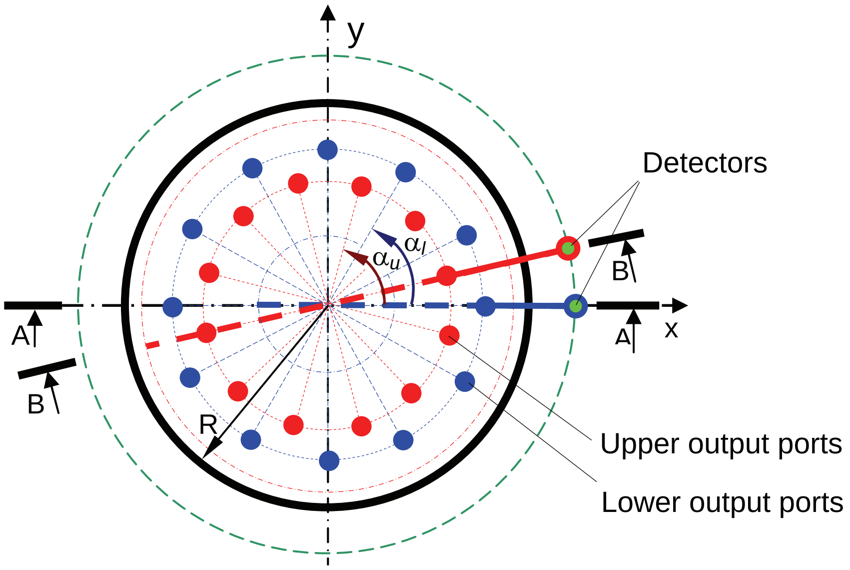

Fig. 2. Schematic of the KMOS Calibrating Unit Integrating Sphere (top view).

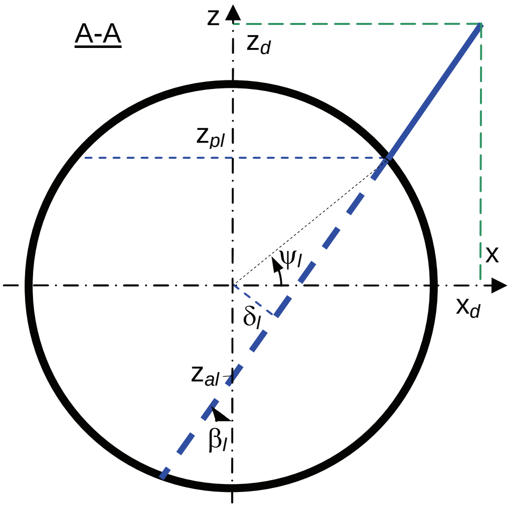

Fig. 3. Schematic of the KMOS Calibrating Unit Integrating Sphere (section A-A).

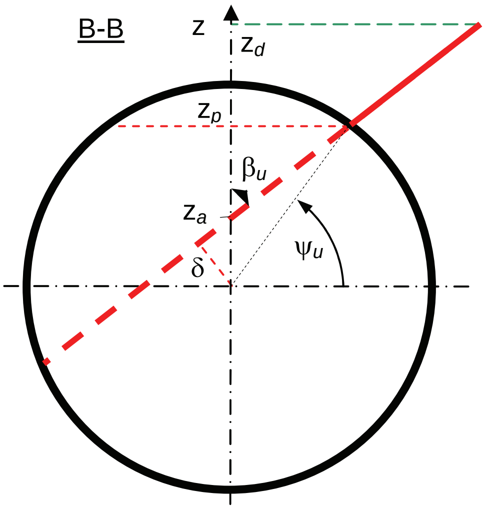

Fig. 4. Schematic of the KMOS Calibrating Unit Integrating Sphere (section B-B).

In order to compute the angular distribution of radiance within the conical solid angle subtended by the upper or lower output port and having the vertex at the detector's position, the following mapping was performed.

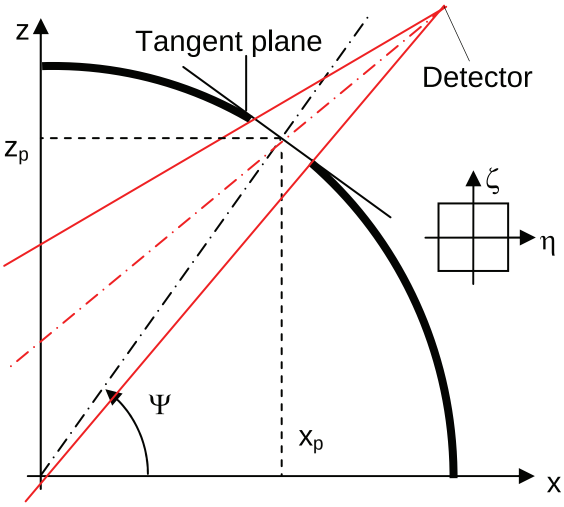

Fig. 5. Scheme of radiance mapping.

We placed a tangent plane on the sphere at the centre of the port under consideration (see Fig. 5) and arranged the local Cartesian coordinate system (η, ζ) so that these local coordinates and global coordinates *(x, y, z)* are connected by relationships:

$$\begin{cases} x = x_p + \zeta \sin\psi = x_p + \dfrac{\zeta \cdot z_p}{R} \\ y = y_p + \eta \\ z = z_p + \zeta \cos\psi = z_p + \dfrac{\zeta \cdot x_p}{R} \end{cases} \tag{2}$$

where (x_p, y_p, z_p) are the global coordinates of an output port. To eliminate the additional coordinate transformations, we aligned the *x* axis with the position of an output port (upper or lower) under consideration and re-computed the positions of all upper and lower output ports. The uniform grid was superimposed on a tangent plane; the radiance values for rays passing through the detector's point and every node of a mesh computed.

5. REFLECTION MODELS

5.1 BRDF definition and properties

The angular radiative properties of an opaque surface can be exhaustively described by the spectral bi-directional reflectance distribution function (BRDF) [7]:

$$f_r(\lambda,\theta_i,\phi_i,\theta_r,\phi_r)=\frac{dL_{\lambda,r}(\lambda,\theta_r,\phi_r)}{dE_{\lambda,i}(\lambda,\theta_i,\phi_i)}=\frac{dL_{\lambda,r}(\lambda,\theta_r,\phi_r)}{L_{\lambda,i}(\lambda,\theta_i,\phi_i)\cos\theta_i d\omega_i}, \tag{3}$$

where λ is wavelength, $L_{\lambda,i}$ is and $L_{\lambda,r}$ are the spectral radiance of incident and reflected radiation, respectively, $E_{\lambda,i}$ is spectral irradiance due to incident radiation, (θ_i,ϕ_i) and (θ_r,ϕ_r) are the spherical coordinates of the directions of incidence and reflection, respectively; $d\omega_i$ is the element of solid angle around the direction of incidence (see Fig. 6).

BRDF has the dimension of sr^{-1}. Directional-hemispherical reflectance can be expressed as an integral over a hemispherical solid angle:

$$\rho(\lambda,\theta_i,\phi_i)=\int_{2\pi} f_r(\lambda,\theta_i,\phi_i,\theta_r,\phi_r)\cos\theta_r\, d\omega_r\,. \tag{4}$$

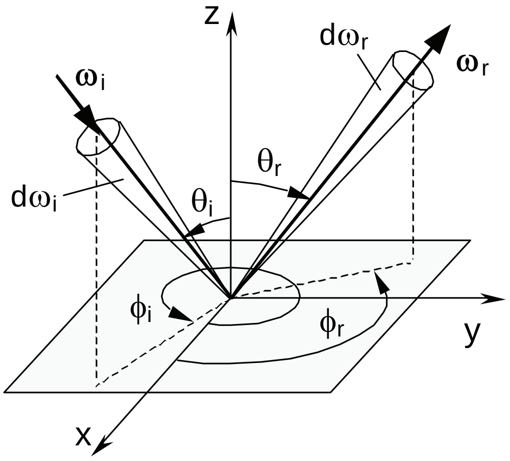

Fig. 6. Definition of BRDF in a spherical coordinate system.

Every BRDF must obey the energy conservation law:

$$\int_{2\pi} f_r(\lambda,\theta_i,\phi_i,\theta_r,\phi_r)\cos\theta_r\, d\omega_r, \quad \forall(\lambda,\theta_i,\phi_i), \tag{5}$$

as well as Helmholtz's reciprocity principle:

$$f_r(\lambda,\theta_i,\phi_i,\theta_r,\phi_r) = f_r(\lambda,\theta_r,\phi_r,\theta_i,\phi_i). \tag{6}$$

Hereinafter, for simplicity, we will use the monochromatic quantities and omit the dependence from wavelength λ. We will also suppose that the radiation is unpolarized and neglect the polarization effects at the reflection.

5.2 Lambertian BRDF

If the radiance of radiation reflected from a surface does not depend on incident nor viewing angle, such a surface obeys Lambert's law (cosine law for radiant intensity); its BRDF is then equal to:

$$f_{Lambert} = \frac{\rho_0}{\pi}, \tag{7}$$

where ρ_0 is the constant normal (or directional-hemispherical) reflectance.

Lambertian BRDF is an idealized model; due to its simplicity, it is widely used at the solution of radiative-transfer problems and could be considered as a zero-order approximation model for this study.

Depending on the computational task, we used not only the conventional method [8] to generate random directions in accordance with a Lambertian BRDF but also a method described in [17]. The conventional method involves computation of the coordinates θ and ϕ of the local spherical coordinate system after simple transformation of a pair of pseudo-random numbers η_θ and η_ϕ, uniformly distributed on (0, 1] segment, according to

$$\theta = \arcsin\sqrt{\eta_\theta}, \quad \phi = 2\pi\eta_\phi, \tag{8}$$

with the subsequent transformations to the local Cartesian coordinate system and then to the global one. An alternative method is based on the following fact: every sphere, which is tangent to the reflecting surface of a Lambertian reflector in the point of reflection, is a surface of uniform irradiance. Therefore, in order to model the sequence of diffuse reflection points on the internal surface of a sphere, it is sufficient to generate the sequence of points uniformly distributed over this surface. The algorithm of G. Marsaglia [9] is used to obtain the points uniformly distributed on the spherical surface $x^2 + y^2 + z^2 = 1$. The next pair of pseudo-random numbers η_x and η_y undergoes the linear transformation

$$u_x = 2\eta_x - 1; \quad u_y = 2\eta_y - 1. \tag{9}$$

The points with coordinates $x = u_x$ and $y = u_y$ are uniformly distributed within the square $(-1 < x, y < 1)$. If $s = u_x^2 + u_y^2 > 1$, a point outside the circle of unit radius, the pair of pseudo-random numbers η_x and η_y is rejected, and new pair is generated. Otherwise, the coordinates of the point on the surface of unit sphere are

$$x = 2u_x\sqrt{1-s}; \quad y = 2u_y\sqrt{1-s}; \quad z = 1-2s. \tag{10}$$

For a sphere of radius *r*, the coordinates of the point in Eq. (10) must be multiplied by the value of *r*. The results of test modeling using both methods are presented in Fig. 7.

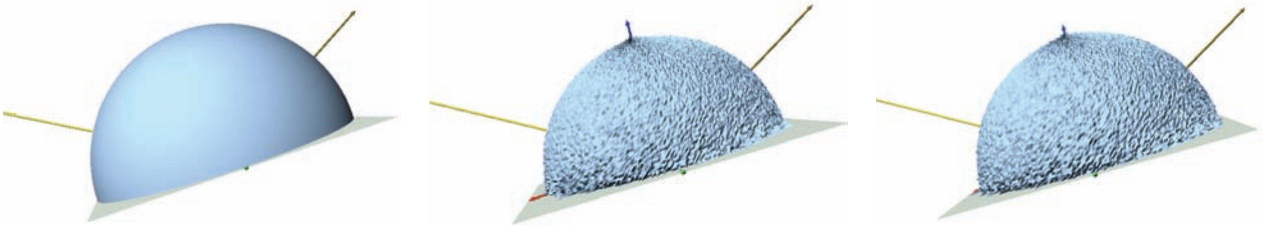

Fig. 7. Lambertian BRDF in spherical coordinates: left – analytic expression; center – conventional method in Monte Carlo modelling, 10^9 rays used; right – Marsaglia's method, 10^9 rays used.

5.3 MRPV BRDF

The semi-empirical BRDF model developed by Rahman, Pinty, and Verstraete [10, 11] for remote sensing applications was modified by Martonchik [12] and then employed for the modelling of Spectralon™ MISR diffusers [13, 14]. The MRPV (Martonchik- Rahman-Pinty-Verstraete) BRDF model has four adjustable parameters and is able to mimic the reflection properties of materials with predominately volumetric scattering such as sintered PTFE, Spectralon™, Halon™ etc.:

$$f_{r,MRPV}\left(\theta_i,\phi_i,\theta_r,\phi_r,A,k,b,\bar{\rho}\right) = A\cdot\left[\cos\theta_i\cos\theta_r\left(\cos\theta_i+\cos\theta_r\right)\right]^{k-1}e^{-bg}\left(1+\frac{\bar{\rho}}{1+G}\right), \tag{11}$$

where *A* is the scaling factor, *A* > 0; *k* is Minnaert exponent, *k* ≥ 0; *b* is asymmetry parameter, $-\infty < b < \infty$; $\bar{\rho}$ is the average reflectance;

$$g = \cos\theta_i\cos\theta_r + \sin\theta_i\sin\theta_r\cos\left(\phi_i-\phi_r\right); \tag{12}$$

$$G = \left[\tan^2\theta_i + \tan^2\theta_r - 2\tan\theta_i\tan\theta_r\cos\left(\phi_i-\phi_r\right)\right]^{1/2}. \tag{13}$$

As a special case at $A=\rho_0, k=1, b=0, \bar{\rho}=0$, MRPV BRDF includes the Lambertian BRDF.

To generate ray directions with the probability density corresponding to MRPV BRDF, the acceptance-rejection method [15] was employed. For every incidence angle θ_i, the high bound value

$$B_h = A\cdot\left[\cos\theta_i\left(1+\cos\theta_i\right)^{k-1}\right]\cdot\frac{2-\bar{\rho}}{\pi} \tag{14}$$

is computed; then the random direction (θ_r, ϕ_r) according to Lambertian BRDF is generated. If, for next random number η, the following inequality

$$\eta \cdot B_h < f_{r,MRPV}(\theta_i, \phi_i, \theta_r, \phi_r, A, k, b, \overline{\rho}), \tag{15}$$

is fulfilled, the direction of reflection (θ_r, ϕ_r) is accepted, otherwise new values of (θ_r, ϕ_r) and η are generated.

6. RAY TRACING ALGORITHM

6.1 Backward ray tracing

Because forward ray tracing (from radiation source to detector) cannot be applied to an estimation of radiance in a given direction or flux in a given point, the backward ray tracing based on the reciprocity principle was used [16].

To model the radiance angular distribution, rays were consecutively traced from the detector through the nodes of the uniform grid covering the output port.

Radiant flux Φ falling onto detector within conical solid angle Ω is equal to

$$\Phi = \int_{\Omega} L(\theta_i) \cos\theta_i d\Omega, \tag{16}$$

where $L(\theta_i)$ is the (spectral) radiance in the direction that forms the angle θ_i with the normal to the surface of a detector.

To compute Φ, we generated the directions uniformly distributed within a solid angle Ω and estimated the integral in Eq. 16.

6.2 Ray-sphere intersection

After determining the global coordinates $(\omega_{rx}, \omega_{ry}, \omega_{rz})$ for the unit vector of the direction of the diffuse reflection $\vec{\omega}_r$, the parametric equations of the reflected ray (primed coordinates belonging to the initial point of a ray),

$$x = x' + \omega_{rx} t; \quad y = y' + \omega_{ry} t; \quad z = z' + \omega_{rz} t, \tag{17}$$

should be solved together with the equation of a sphere $x^2 + y^2 + z^2 = R^2$ to determine the value of the parameter t. If initial point (x', y', z') lies on the sphere,

$$t = -2 \cdot \left(x'\omega_{rx} + y'\omega_{ry} + z'\omega_{rz} \right). \tag{18}$$

then the coordinates (x, y, z) can be found. After each reflection, the radiance of a ray is multiplied by the value of reflectance at the angle of incidence. Ray tracing ends when a ray escapes the sphere through one of openings, or when the energy carried by the ray becomes less than the prescribed threshold value.

6.3 Shadow rays method

To accelerate the convergence of computational process, we used the so-called "shadow rays" method that was described in details in [17, 18] for Lambertian sphere walls. We have expanded this method for non-Lambertian surfaces.

The shadow rays method implies computation of income due to source direct radiation into radiance in each point of reflection. In our case, the collimated beam with uniform distribution of optical energy over the beam section irradiates the sphere area that is considered as a secondary source. The radiance of radiation, reflected from this area is connected with the irradiance due to the initial collimated beam by the relationships (subscript "s" is for source):

$$dL_s\left(\theta_{s,r}, \phi_{sr}\right) = f\left(\theta_{si}, \phi_{si}, \theta_{sr}, \phi_{sr}\right) dE\left(\theta_{si}, \phi_{si}\right), \tag{19}$$

$$L_s = \int_S f\left(\theta_{s,i}, \phi_{s,i}, \theta_{s,r}, \phi_{s,r}\right) \cdot dE\left(\theta_{s,i}, \phi_{s,i}\right) = Const \cdot f\left(\theta_{s,i}, \phi_{s,i}, \theta_{s,r}, \phi_{s,r}\right), \tag{20}$$

The income of the source into radiance reflected by a point on the sphere:

$$\begin{aligned} L_{rs} &= \int_\Omega L_s f\left(\theta_{r,i}, \phi_{r,i}, \theta_{r,r}, \phi_{r,r}\right) \cos\theta_{r,i} d\omega_i = \\ &Const \cdot f\left(\theta_{s,i}, \phi_{s,i}, \theta_{s,r}, \phi_{s,r}\right) \cdot f\left(\theta_{r,i}, \phi_{r,i}, \theta_{r,r}, \phi_{r,r}\right) \frac{\cos\theta_{r,i} \cdot \cos\theta_{s,r}}{d_{sr}^2} \end{aligned} \tag{21}$$

Since all rays of a collimated beam carry the same energy, we can assume that Const = 1.

The radiance of a ray incident on the detector (see Fig. 8) can be expressed as

$$\begin{aligned} &\rho(\theta_1')\left(f\left(\theta_{s,i}, \phi_{s,i}, \theta_{s,r}, \phi_{s,r}\right) \cdot f\left(\theta_{r,i}, \phi_{r,i}, \theta_{r,r}, \phi_{r,r}\right) \frac{\cos\theta_{r,i} \cdot \cos\theta_{s,r}}{d_{sr}^2} \right)_1 + \\ &\rho(\theta_2')\rho(\theta_1')\left(f\left(\theta_{s,i}, \phi_{s,i}, \theta_{s,r}, \phi_{s,r}\right) \cdot f\left(\theta_{r,i}, \phi_{r,i}, \theta_{r,r}, \phi_{r,r}\right) \frac{\cos\theta_{r,i} \cdot \cos\theta_{s,r}}{d_{sr}^2} \right)_2 + \\ &\rho(\theta_3')\rho(\theta_2')\rho(\theta_1')\left(f\left(\theta_{s,i}, \phi_{s,i}, \theta_{s,r}, \phi_{s,r}\right) \cdot f\left(\theta_{r,i}, \phi_{r,i}, \theta_{r,r}, \phi_{r,r}\right) \frac{\cos\theta_{r,i} \cdot \cos\theta_{s,r}}{d_{sr}^2} \right)_3 + \ldots = \\ &\rho(\theta_1')\left(L_{s1} + \rho(\theta_2')\left(L_{s2} + \rho(\theta_3')\left(L_{s3} + \rho(\theta_4')\left(L_{s4} + \ldots\right)\right)\right)\right) = \\ &\sum_{k=1}^{n} \left(f\left(\theta_{s,i}, \phi_{s,i}, \theta_{s,r}, \phi_{s,r}\right) \cdot f\left(\theta_{r,i}, \phi_{r,i}, \theta_{r,r}, \phi_{r,r}\right) \frac{\cos\theta_{r,i} \cdot \cos\theta_{s,r}}{d_{sr}^2} \right)_k \prod_{j=1}^{k} \rho(\theta_j') \end{aligned} \tag{22}$$

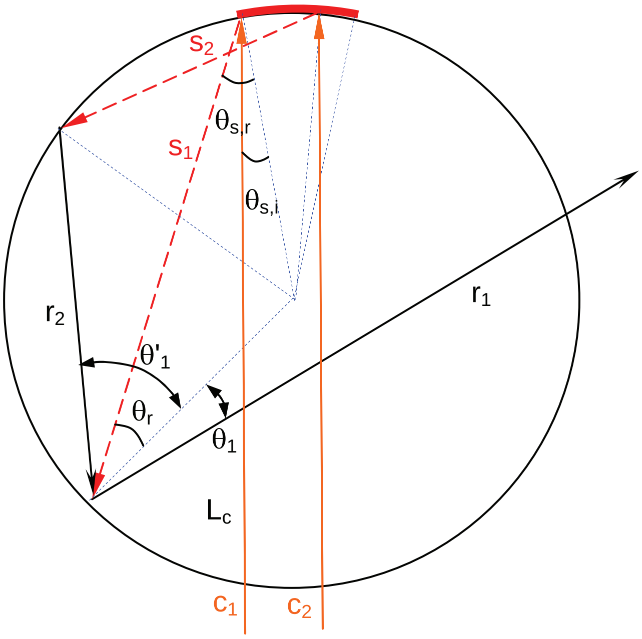

Fig. 8. The schematic of shadow rays method.

6.4 Method of depending trials

The method of depending trials (or by another name – the method of correlated sampling) [19, 20] allows results to be obtained for several (spectral) reflectances of sphere wall simultaneously, using the same set of ray trajectories. It is assumed that the shape of the BRDF does not change. For MRPV BRDF this means that the scaling factor *A* can consist of several components $(A_1, A_2, ..., A_m)$.

7. RESULTS OF NUMERICAL EXPERIMENTS

7.1 Initial geometrical data

All geometrical parameters used for modelling are shown in Table 1.

Table 1. Initial geometrical parameters (linear dimensions are in mm, angular in deg.)

Parameter	***Value***	***Comments***
Number of Upper Output Ports, N_u	12	
Number of Lower Output Ports, N_l	12	
Sphere Internal Radius, R	90	
Input Port Radius, R_{ip}	5	
Collimated Beam Radius, R_{cb}	4.9	Variable, from 0.1 mm to 4.9 mm
Equator-to-FOV Vertex Distance, H_d	176.4	
Z Axis-to-FOV Vertex Distance, L_d	139.5	
Output Port Radius, R_{op}	9	Each port is formed as a section of the sphere by the right circular cylinder, whose axis passes through the sphere centre
Upper FOV Axis-to-Sphere Centre Distance, δ_u	28.587	
Lower FOV Axis-to-Sphere Centre Distance, δ_l	23.775	
Upper FOV Axis-to-Z Axis Angle, β_u	45.64	
Lower FOV Axis-to-Z Axis Angle, β_l	32.27	
Upper FOV Vertex Angle, Ω_u	5.72	f/10 case
Lower FOV Vertex Angle, Ω_l	5.72	f/10 case

7.2 Four BRDF models

After analyzing the available published data on sintered PTFE BRDF [13, 14, 21, 22], we selected four BRDF models:

Model 0. Lambertian BRDF; method of depending trials allows the simultaneous modelling of the sphere walls with $\rho_0 =$0.95, 0.96, 0.97, 0.98, and 0.99. This is the zero approximation model.

Model 1. MRPV BRDF with parameters A = 0.956336, 0.966403, 0.976470, 0.986536, 0.996603; k = 1.01; b = 0.01; $\overline{\rho} = 1$. The components of A were chosen so that normal reflectance $\rho_n = \rho(0) =$0.95, 0.96, 0.97, 0.98, and 0.99. This is the "optimistic" model.

Model 2. MRPV BRDF with parameters A = 0.962708, 0.972841, 0.982975, 0.993109, 1.003243; k = 1.02; b = 0.02; $\overline{\rho} = 1$. The components of A were also chosen so that normal reflectance $\rho_n = \rho(0) =$0.95, 0.96, 0.97, 0.98, and 0.99. This is the "pessimistic" model.

Model 3. MPRV BRDF with parameters *A* = 1.081842, 1.093230, 1.104618, 1.116006, 1.127394; *k* = 1.2; *b* = 0.2; $\bar{\rho} = 1$. The components of *A* were also chosen so that normal reflectance $\rho_n = \rho(0) = 0.95$, 0.96, 0.97, 0.98, and 0.99. This model is a far-from-Lambertian one and was used only to demonstrate the efficacy of the algorithm and code.

3-Dimensional representations of the model BRDFs in a spherical coordinate system for three incidence angles are depicted in Fig. 9. Their sections by the plane of incidence are shown in Fig. 10.

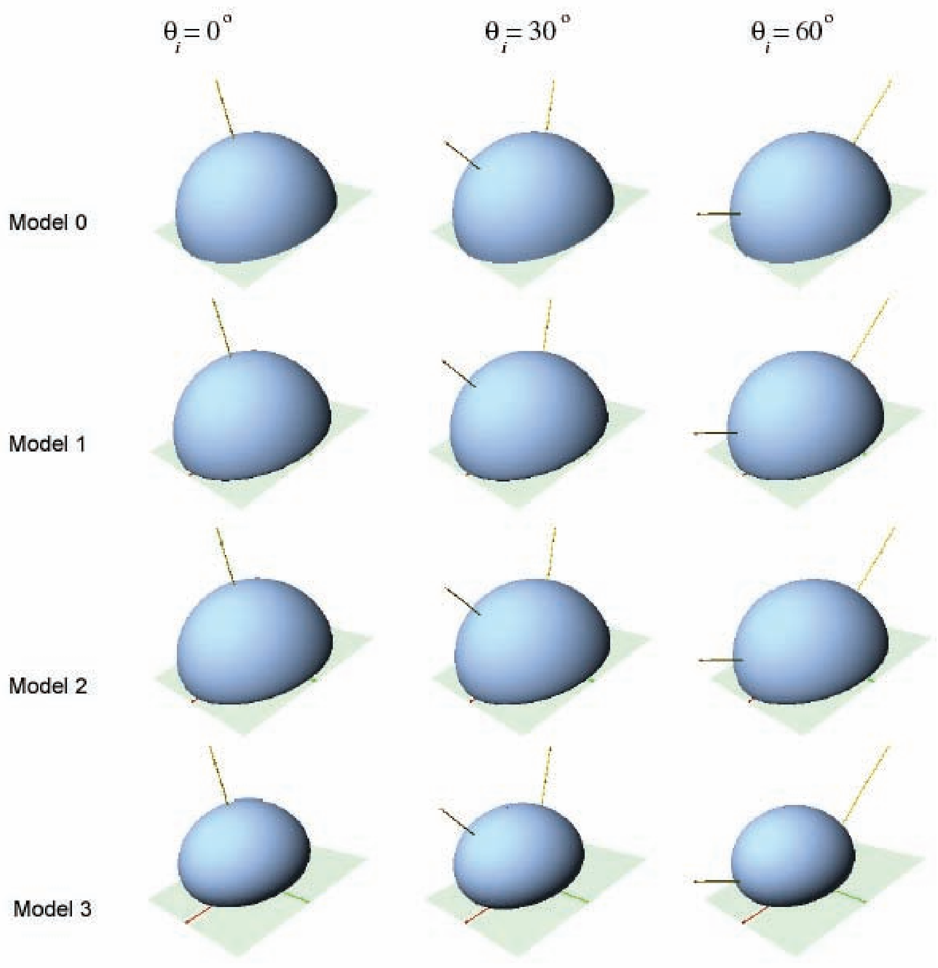

Fig. 9. 3-D images of BRDF models in a spherical coordinate system for three values of incidence angle

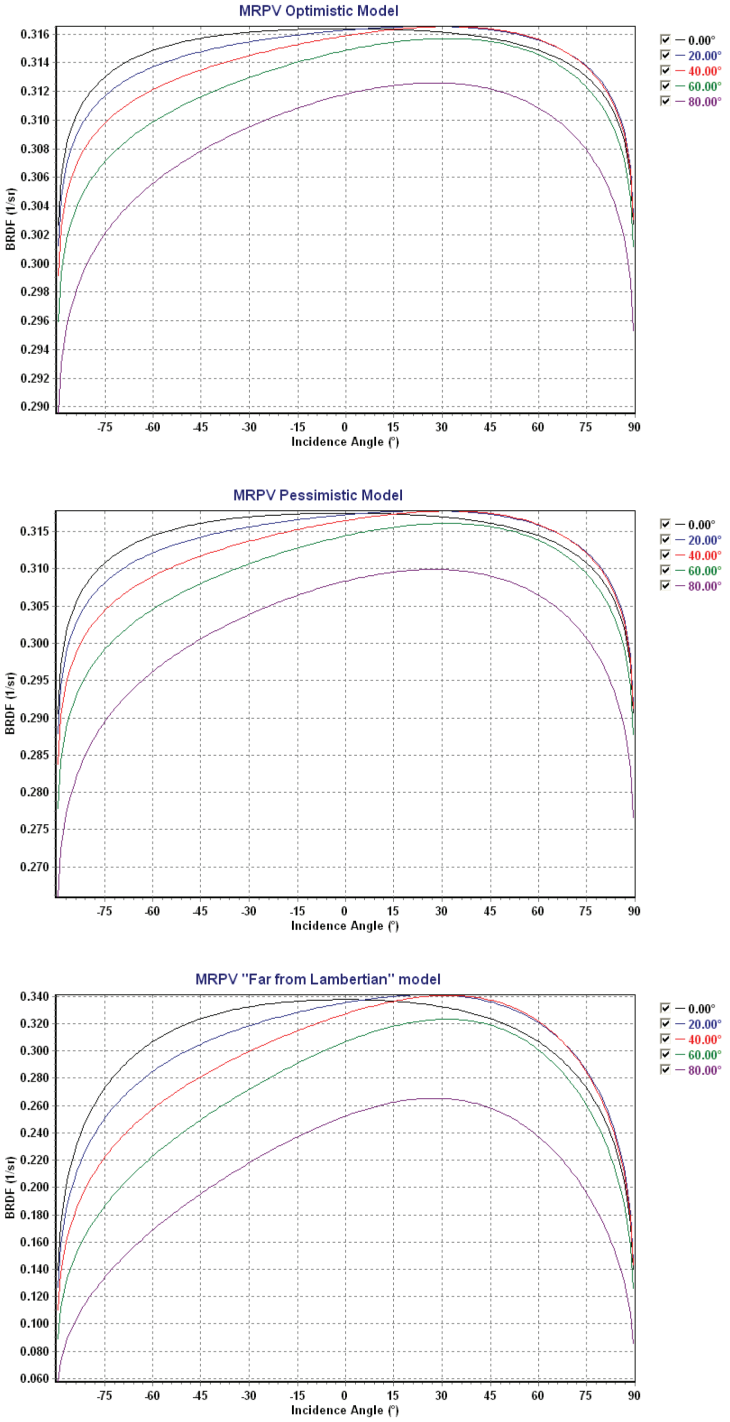

Fig. 10. BRDF Models 1, 2, and 3 for θ_i = 0°, 20°, 40°, 60° and 80° in plane of incidence

The directional-hemispherical reflectances of the BRDF Models 1, 2, and 3 were computed by numerical integration of the appropriate BRDFs and plotted against incidence angle (see Fig. 11).

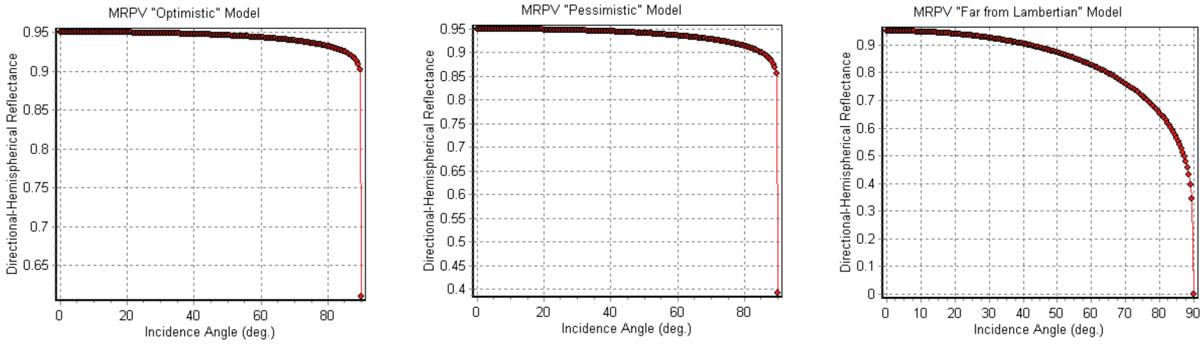

Fig. 11. Directional-hemispherical reflectances of BRDF Models 1, 2, and 3 plotted against incidence angle

7.3 Lambertian BRDF. Evaluation of computational accuracy

Colour maps of the relative distributions of radiance over the upper (left-hand maps) and lower (right-hand maps) ports are presented in Figures 12 – 23. The standard deviation from the mean value is shown at the top of each map, computed for a very coarse grid having 9 × 9 nodes. For each node, 10^6 rays were traced.

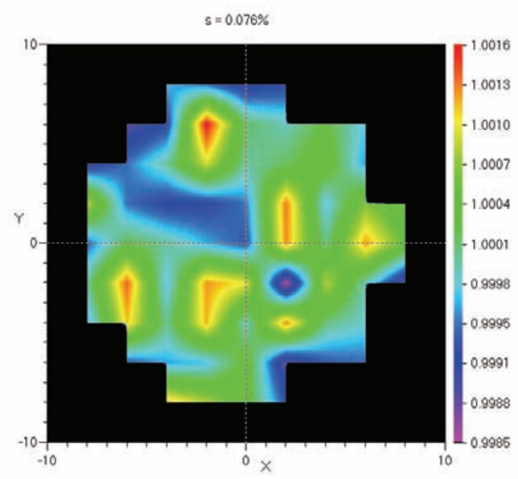

Fig. 12. Upper port; $\rho_0 = 0.95$.

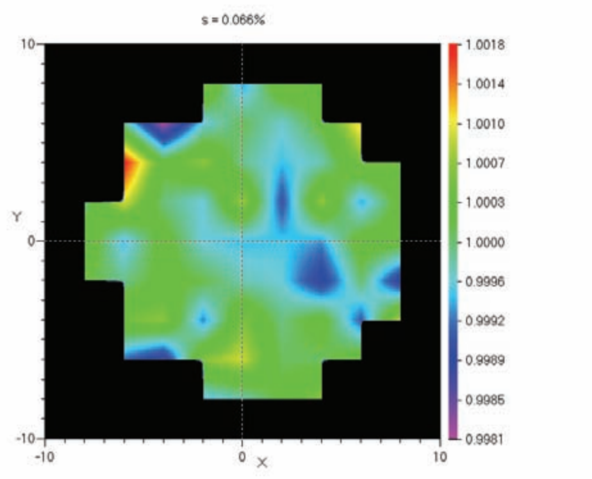

Fig. 13. Lower port; $\rho_0 = 0.95$.

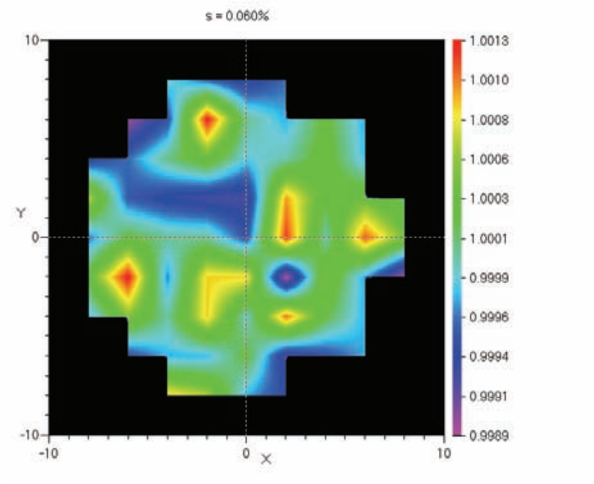

Fig. 14. Upper port; $\rho_0 = 0.96$.

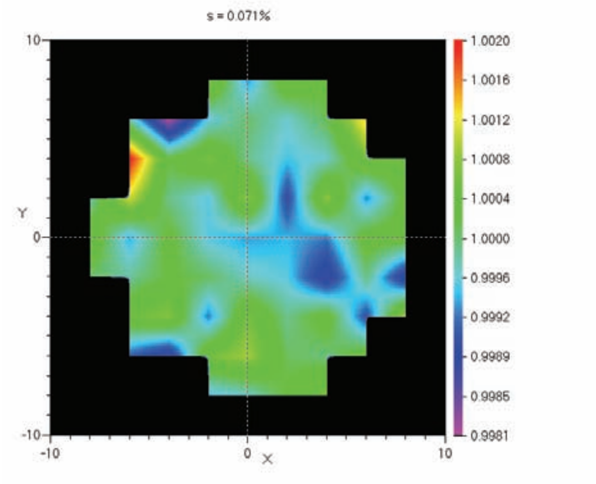

Fig. 15. Lower port; $\rho_0 = 0.96$.

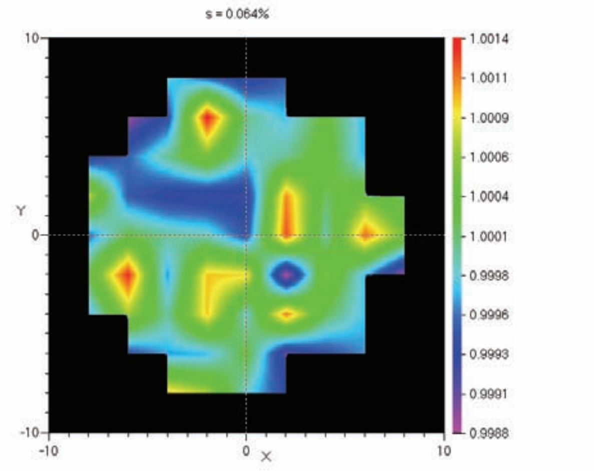

Fig. 16. Upper port; $\rho_0 = 0.97$.

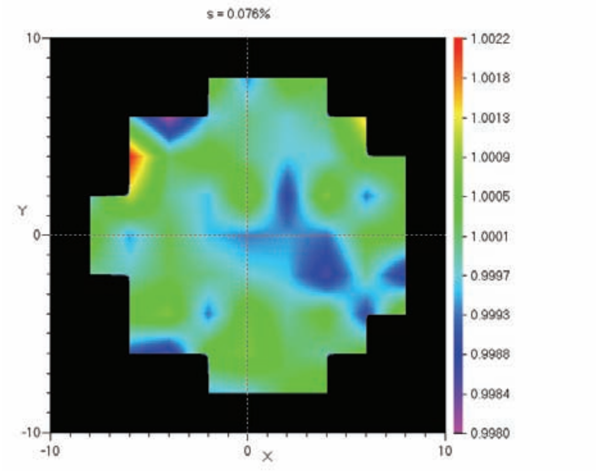

Fig. 18. Lower port; $\rho_0 = 0.97$.

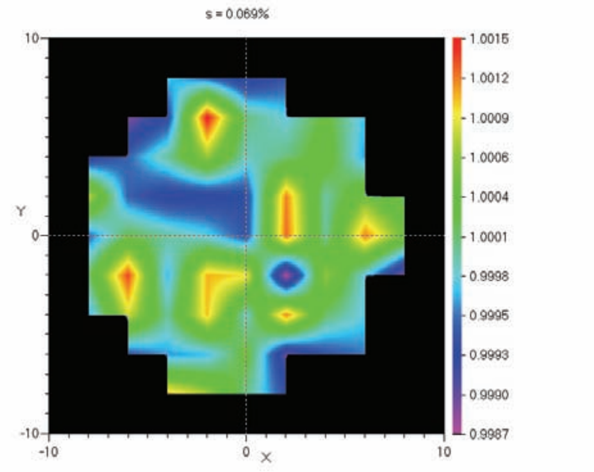

Fig. 19. Upper port; $\rho_0 = 0.98$.

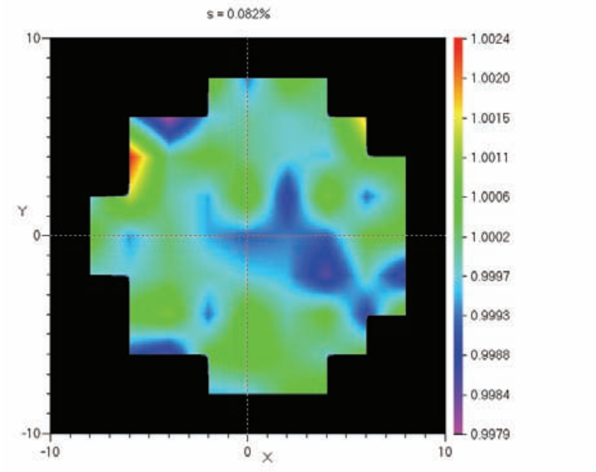

Fig. 20. Lower port; $\rho_0 = 0.98$.

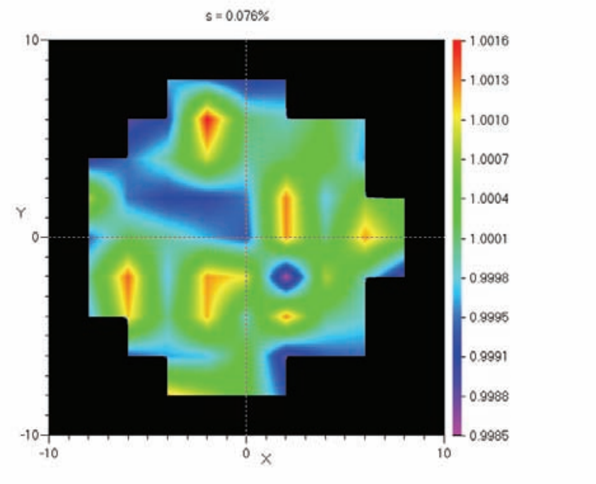

Fig. 21. Upper port; $\rho_0 = 0.99$.

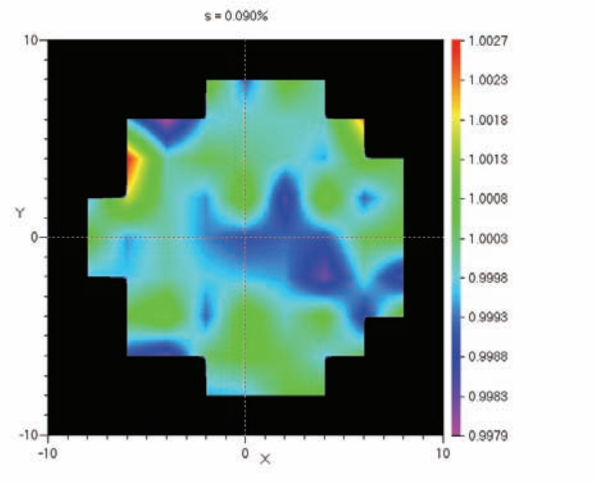

Fig. 22. Lower port; $\rho_0 = 0.99$.

The radiance distributions depicted in the Figures 12 – 22 exhibit no regular structure. We performed additional numerical experiments for $N_r = 10^7$ and 10^8 rays traced. It was found that the value of standard deviation decreases as $N_r^{-\frac{1}{2}}$ with the N_r increased. This means that the standard deviation characterizes the random digital noise, and the radiance distribution is uniform (within the framework of Lambertian approximation).

We obtained the trivial result that could be obtained without numerical modelling. Indeed, if an integrating sphere with Lambertian walls does not include baffles or other auxiliary elements, one can predict the uniformity of radiance distribution over the whole sphere surface except for an initially irradiated area. Openings of arbitrary number and shape can decrease the mean level of radiance but cannot violate the uniformity of distribution. Because the configuration factor between two arbitrary points on the internal surface of Lambertian sphere depends only on sphere radius, the incident flux is the same for the entire sphere surface, as well as radiation losses through the openings being the same.

This is good example of a case when simple Lambertian model of reflection is insufficient. However, the numerical experiments performed allow the evaluaton of the standard deviation of random uncertainty of computations: about 0.08% for 10^6 rays traced and about 0.02% for 10^7 rays.

7.4 Angular distributions of radiance for MRPV BRDF

Computer modelling with MRPV BRDF is several times slower than that for Lambertian BRDF. To save time, we abandoned the modelling of 2D radiance mapping even on a coarse grid. Due to the quasi-symmetry of full system around the z axis, one can predict that the radiance gradient in a vertical direction will be greater than that in a horizontal direction. Accordingly, we modelled only one-dimensional distributions in horizontal and vertical directions, across the centre of upper and lower ports. The results of the modelling are presented in Tables 2 – 7 and in Fig. 23. All results were obtained with 10^6 traced rays.

Table 2. MRPV BRDF Model 1, vertical scan.

y (mm)	Upper Port, for Normal Reflectance					Lower Port, for Normal Reflectance				
	0.95	0.96	0.97	0.98	0.99	0.95	0.96	0.97	0.98	0.99
-8	2.308E-05	2.589E-05	2.926E-05	3.336E-05	3.845E-05	2.308E-05	2.589E-05	2.926E-05	3.336E-05	3.845E-05
-6	2.306E-05	2.587E-05	2.923E-05	3.333E-05	3.841E-05	2.306E-05	2.587E-05	2.923E-05	3.332E-05	3.840E-05
-4	2.307E-05	2.588E-05	2.924E-05	3.334E-05	3.844E-05	2.306E-05	2.587E-05	2.924E-05	3.333E-05	3.842E-05
-2	2.309E-05	2.590E-05	2.927E-05	3.337E-05	3.846E-05	2.305E-05	2.586E-05	2.922E-05	3.331E-05	3.839E-05
0	2.306E-05	2.587E-05	2.924E-05	3.333E-05	3.843E-05	2.306E-05	2.587E-05	2.923E-05	3.332E-05	3.840E-05
2	2.308E-05	2.589E-05	2.926E-05	3.335E-05	3.845E-05	2.307E-05	2.588E-05	2.924E-05	3.334E-05	3.842E-05
4	2.305E-05	2.586E-05	2.922E-05	3.332E-05	3.841E-05	2.308E-05	2.590E-05	2.927E-05	3.337E-05	3.846E-05
6	2.306E-05	2.587E-05	2.923E-05	3.333E-05	3.841E-05	2.306E-05	2.587E-05	2.923E-05	3.333E-05	3.841E-05
8	2.307E-05	2.588E-05	2.924E-05	3.334E-05	3.843E-05	2.308E-05	2.589E-05	2.926E-05	3.337E-05	3.846E-05
Std. Dev.	0.054%	0.053%	0.052%	0.050%	0.047%	0.051%	0.055%	0.060%	0.065%	0.071%

Table 3. MRPV BRDF Model 1, horizontal scan.

x (mm)	Upper Port, for Normal Reflectance					Lower Port, for Normal Reflectance				
	0.95	0.96	0.97	0.98	0.99	0.95	0.96	0.97	0.98	0.99
-8	2.306E-05	2.587E-05	2.923E-05	3.332E-05	3.841E-05	2.306E-05	2.586E-05	2.922E-05	3.332E-05	3.840E-05
-6	2.307E-05	2.588E-05	2.925E-05	3.335E-05	3.845E-05	2.309E-05	2.590E-05	2.927E-05	3.337E-05	3.846E-05
-4	2.303E-05	2.584E-05	2.920E-05	3.328E-05	3.836E-05	2.307E-05	2.588E-05	2.924E-05	3.333E-05	3.842E-05
-2	2.305E-05	2.586E-05	2.922E-05	3.331E-05	3.840E-05	2.306E-05	2.587E-05	2.924E-05	3.333E-05	3.841E-05
0	2.305E-05	2.585E-05	2.922E-05	3.331E-05	3.840E-05	2.306E-05	2.587E-05	2.923E-05	3.332E-05	3.840E-05
2	2.303E-05	2.584E-05	2.920E-05	3.329E-05	3.836E-05	2.308E-05	2.589E-05	2.926E-05	3.336E-05	3.845E-05
4	2.303E-05	2.584E-05	2.919E-05	3.328E-05	3.835E-05	2.306E-05	2.587E-05	2.923E-05	3.333E-05	3.841E-05
6	2.306E-05	2.587E-05	2.923E-05	3.333E-05	3.841E-05	2.307E-05	2.588E-05	2.924E-05	3.334E-05	3.843E-05
8	2.303E-05	2.584E-05	2.920E-05	3.328E-05	3.836E-05	2.305E-05	2.586E-05	2.922E-05	3.331E-05	3.838E-05
Std. Dev.	0.060%	0.065%	0.070%	0.076%	0.083%	0.042%	0.047%	0.052%	0.059%	0.067%

Table 4. MRPV BRDF Model 2, vertical scan.

y (mm)	Upper Port, for Normal Reflectance					Lower Port, for Normal Reflectance				
	0.95	0.96	0.97	0.98	0.99	0.95	0.96	0.97	0.98	0.99
-8	2.217E-05	2.478E-05	2.788E-05	3.162E-05	3.620E-05	2.218E-05	2.479E-05	2.790E-05	3.164E-05	3.624E-05
-6	2.221E-05	2.482E-05	2.793E-05	3.168E-05	3.628E-05	2.217E-05	2.478E-05	2.788E-05	3.162E-05	3.620E-05
-4	2.218E-05	2.479E-05	2.789E-05	3.163E-05	3.622E-05	2.219E-05	2.480E-05	2.790E-05	3.165E-05	3.625E-05
-2	2.218E-05	2.479E-05	2.789E-05	3.163E-05	3.623E-05	2.219E-05	2.480E-05	2.790E-05	3.164E-05	3.623E-05
0	2.216E-05	2.477E-05	2.787E-05	3.160E-05	3.619E-05	2.218E-05	2.479E-05	2.789E-05	3.163E-05	3.622E-05
2	2.214E-05	2.474E-05	2.784E-05	3.157E-05	3.616E-05	2.217E-05	2.478E-05	2.787E-05	3.161E-05	3.619E-05
4	2.216E-05	2.477E-05	2.787E-05	3.162E-05	3.622E-05	2.220E-05	2.482E-05	2.792E-05	3.166E-05	3.625E-05
6	2.213E-05	2.474E-05	2.783E-05	3.156E-05	3.614E-05	2.222E-05	2.483E-05	2.794E-05	3.169E-05	3.629E-05
8	2.217E-05	2.478E-05	2.788E-05	3.162E-05	3.621E-05	2.220E-05	2.481E-05	2.791E-05	3.165E-05	3.625E-05
Std. Dev.	0.100%	0.102%	0.104%	0.107%	0.110%	0.066%	0.069%	0.072%	0.076%	0.082%

Table 5. MRPV BRDF Model 2, horizontal scan.

x (mm)	Upper Port, for Normal Reflectance					Lower Port, for Normal Reflectance				
	0.95	0.96	0.97	0.98	0.99	0.95	0.96	0.97	0.98	0.99
-8	2.218E-05	2.479E-05	2.790E-05	3.165E-05	3.625E-05	2.219E-05	2.480E-05	2.791E-05	3.165E-05	3.625E-05
-6	2.217E-05	2.478E-05	2.788E-05	3.162E-05	3.621E-05	2.219E-05	2.480E-05	2.790E-05	3.164E-05	3.623E-05
-4	2.217E-05	2.478E-05	2.788E-05	3.163E-05	3.622E-05	2.219E-05	2.480E-05	2.790E-05	3.164E-05	3.623E-05
-2	2.217E-05	2.478E-05	2.789E-05	3.163E-05	3.623E-05	2.216E-05	2.477E-05	2.786E-05	3.159E-05	3.618E-05
0	2.216E-05	2.477E-05	2.788E-05	3.162E-05	3.621E-05	2.219E-05	2.481E-05	2.791E-05	3.165E-05	3.625E-05
2	2.217E-05	2.478E-05	2.788E-05	3.162E-05	3.621E-05	2.217E-05	2.477E-05	2.787E-05	3.160E-05	3.619E-05
4	2.217E-05	2.478E-05	2.789E-05	3.163E-05	3.622E-05	2.217E-05	2.478E-05	2.788E-05	3.161E-05	3.620E-05
6	2.213E-05	2.474E-05	2.783E-05	3.156E-05	3.615E-05	2.217E-05	2.477E-05	2.787E-05	3.161E-05	3.620E-05
8	2.216E-05	2.477E-05	2.787E-05	3.161E-05	3.620E-05	2.219E-05	2.481E-05	2.791E-05	3.165E-05	3.625E-05
Std. Dev.	0.059%	0.063%	0.067%	0.072%	0.077%	0.056%	0.061%	0.066%	0.073%	0.080%

Table 6. MRPV BRDF Model 3, vertical scan.

y (mm)	Upper Port, for Normal Reflectance					Lower Port, for Normal Reflectance				
	0.95	0.96	0.97	0.98	0.99	0.95	0.96	0.97	0.98	0.99
-8	1.442E-05	1.559E-05	1.689E-05	1.834E-05	1.996E-05	1.428E-05	1.543E-05	1.671E-05	1.814E-05	1.974E-05
-6	1.441E-05	1.558E-05	1.688E-05	1.833E-05	1.996E-05	1.440E-05	1.556E-05	1.685E-05	1.829E-05	1.991E-05
-4	1.431E-05	1.547E-05	1.676E-05	1.820E-05	1.982E-05	1.436E-05	1.552E-05	1.681E-05	1.824E-05	1.986E-05
-2	1.432E-05	1.548E-05	1.678E-05	1.822E-05	1.985E-05	1.446E-05	1.562E-05	1.692E-05	1.837E-05	1.999E-05
0	1.420E-05	1.536E-05	1.664E-05	1.808E-05	1.969E-05	1.443E-05	1.560E-05	1.689E-05	1.833E-05	1.995E-05
2	1.420E-05	1.536E-05	1.665E-05	1.809E-05	1.970E-05	1.449E-05	1.566E-05	1.696E-05	1.841E-05	2.003E-05
4	1.404E-05	1.519E-05	1.646E-05	1.789E-05	1.949E-05	1.448E-05	1.565E-05	1.695E-05	1.840E-05	2.002E-05
6	1.421E-05	1.536E-05	1.665E-05	1.808E-05	1.969E-05	1.446E-05	1.562E-05	1.692E-05	1.837E-05	1.999E-05
8	1.438E-05	1.555E-05	1.684E-05	1.829E-05	1.991E-05	1.451E-05	1.568E-05	1.698E-05	1.844E-05	2.006E-05
Std. Dev.	0.867%	0.848%	0.828%	0.809%	0.790%	0.506%	0.506%	0.505%	0.505%	0.505%

Table 7. MRPV BRDF Model 3, horizontal scan.

x (mm)	Upper Port, for Normal Reflectance					Lower Port, for Normal Reflectance				
	0.95	0.96	0.97	0.98	0.99	0.95	0.96	0.97	0.98	0.99
-8	1.424E-05	1.540E-05	1.669E-05	1.813E-05	1.975E-05	1.444E-05	1.561E-05	1.690E-05	1.835E-05	1.997E-05
-6	1.421E-05	1.537E-05	1.666E-05	1.810E-05	1.972E-05	1.444E-05	1.560E-05	1.690E-05	1.835E-05	1.997E-05
-4	1.420E-05	1.536E-05	1.665E-05	1.809E-05	1.970E-05	1.442E-05	1.558E-05	1.687E-05	1.832E-05	1.993E-05
-2	1.420E-05	1.536E-05	1.664E-05	1.808E-05	1.969E-05	1.443E-05	1.559E-05	1.689E-05	1.833E-05	1.995E-05
0	1.419E-05	1.535E-05	1.663E-05	1.807E-05	1.968E-05	1.443E-05	1.560E-05	1.689E-05	1.833E-05	1.995E-05
2	1.419E-05	1.535E-05	1.663E-05	1.807E-05	1.968E-05	1.443E-05	1.560E-05	1.689E-05	1.834E-05	1.996E-05
4	1.419E-05	1.535E-05	1.663E-05	1.807E-05	1.968E-05	1.443E-05	1.560E-05	1.689E-05	1.834E-05	1.996E-05
6	1.421E-05	1.537E-05	1.666E-05	1.810E-05	1.971E-05	1.443E-05	1.559E-05	1.689E-05	1.833E-05	1.995E-05
8	1.421E-05	1.537E-05	1.666E-05	1.810E-05	1.971E-05	1.444E-05	1.560E-05	1.690E-05	1.834E-05	1.996E-05
Std. Dev.	0.105%	0.109%	0.112%	0.116%	0.120%	0.049%	0.050%	0.052%	0.053%	0.054%

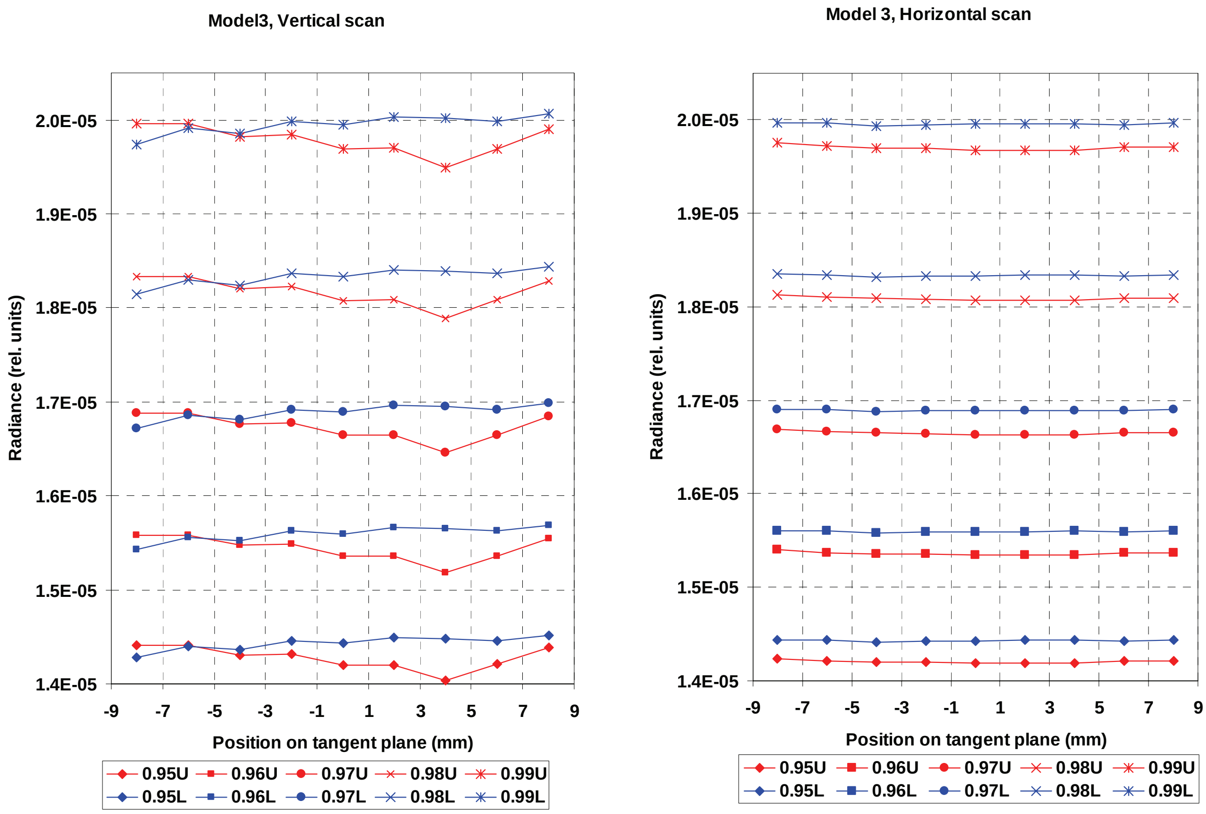

Fig. 23. MRPV BRDF Model 3; vertical and horizontal scans of radiance distributions; "U" and "L" after normal reflectance values in the legends indicate upper and lower output ports, respectively.

7.5 Radiant fluxes difference

We computed the radiant fluxes falling onto a detector within a conical solid angle with the angle at a vertex of 5.72º (f/10 case). The relative difference between the results for upper and lower ports was computed as

$$\gamma = \frac{100\% \cdot (\Phi_u - \Phi_l)}{(\Phi_u + \Phi_l)/2}, \tag{23}$$

where subscripts "*u*" and "*l*" denote upper and lower ports, respectively.

It was found that the convergence of the computational process for radiant flux is 5 to 10 times faster than that for radiance. The results of modelling are presented in Table 8.

Table 8. Relative difference γ between radiant fluxes from upper and lower ports.

Sphere wall normal reflectance	**γ (%)**		
	Model 1	*Model 2*	*Model 3*
0.95	-0.004%	-0.127%	-1.237%
0.96	0.002%	-0.121%	-1.169%
0.97	0.008%	-0.114%	-1.100%
0.98	0.013%	-0.108%	-1.032%
0.99	0.018%	-0.102%	-0.963%

The numerical experiments show a weak dependence of radiant flux difference upon the radius of the incident collimated beam that cannot have practical importance.

8. CONCLUSIONS

1. The Lambertian model of reflection is too crude an approximation for solving the problem stated.
2. On the basis of a MRPV BRDF model and shadow rays method, the versatile algorithm of Monte Carlo ray tracing is developed; it allows the computing of the radiance distributions and radiant fluxes with a random uncertainty of several hundredths of a percent.
3. For several physically plausible BRDF models of sintered PTFE, the non-uniformities of radiance distributions over the upper and lower output ports were computed. It is shown, that, depending on the sphere wall BRDF, non-uniformity over each port could be within the range from 0.05% to 0.1%; the relative difference of the mean radiance between upper and lower ports is about 0.2%. The relative difference of appropriate radiant fluxes is not greater than 0.13%.
4. All above-mentioned results must be considered as a preliminary assessment only. They should be refined after accurate measurements of the BRDF of the chosen sphere material have been made.

9. REFERENCES

1. M. W. Finkel, Integrating sphere theory. Opt. Commun. **2**, 25-28 (1970).
2. R. L. Brown, A numerical solution of the integral equation describing a photometric integrating sphere, Journ. Res. Nat. Bureau of Standards, A. Physics and Chemistry, **77A**, 343-351 (1973).
3. Y. Ohno, Integrating sphere simulation: application to total flux scale realization, Appl. Opt., **33**, 2637–2646 (1994).
4. A. Prokhorov, S. Mekhontsev, L.Hanssen. Evaluation of performance of integrating spheres for indirect emittance measurement. Proc. of 8th International Symposium on Temperature and Thermal Measurements in Industry and Science. Vol. 1. 19-21 June 2001, Berlin, Germany, pp. 277-282
5. L. M. Hanssen, Effects of non-Lambertian surfaces on integrating sphere measurements, Appl. Opt. **35**, 3597-3606 (1996).

6. A. Ziegler, H. Hess, H. Schimpl, Rechnersimulation von Ulbrichtkugeln, Optik, **101**, 130-136 (1996).
7. F. E. Nicodemus et al., Geometrical considerations and Nomenclature for Reflectance, NBS Monograph 160, US Department of Commerce, National Bureau of Standards (1977).
8. R. Siegel, J. R. Howell, Thermal Radiation Heat Transfer. 3rd Ed., Taylor & Francis, Washington, DC (1992).
9. G. Marsaglia, Choosing a point from the surface of a sphere, The Annals of Math. Statistics, **43**, 645-646 (1972).
10. Rahman H., Verstraete M.M., Pinty B. Coupled Surface-Atmosphere Reflectance (CSAR) Model. 1. Model description and inversion of synthetic data. Journal of Geophysical Research, 1993, **98**, D11, 20779-20789
11. Rahman H., Pinty B., Verstraete M.M. Coupled Surface-Atmosphere Reflectance (CSAR) Model. 2. Semiempirical surface model usable with NOAA Advanced Very High Resolution Radiometer Data. Journal of Geophysical Research, 1993, **98**, D11, 20791-20801
12. Engelsen, O., B. Pinty, M. M. Verstraete, and J. V. Martonchik. Parametric Bidirectional Reflectance Factor Models: Evaluation, Improvements and Applications, EC Joint Research Centre, Technical Report No. EUR 16426 EN, 114 p., 1996
13. S. P. Flasse, M. M. Verstraete, B. Pinty, C. J. Bruegge. Modeling Spectralon's bidirectional reflectance for in-flight calibration of Earth-orbiting sensors. Proc. SPIE, vol. 1938, 100-108 (1993)
14. C. J. Bruegge, N. Chrien, D. Haner. A Spectralon BRF data base for MISR calibration applications. Remote Sens. Environ., v. 77, 354-366 (2001)
15. Dagpunar J. Principles of Random Variate Generation. Clarendon Press, Oxford, 1988
16. P. Shirley, Realistic Ray Tracing, A K Peters, Natick, MA (2000).
17. A. V. Prokhorov, S. N. Mekhontsev, and L. M. Hanssen. Monte Carlo modeling of an integrating sphere reflectometer. Applied Optics, v. 42, No. 19, 3832-3842 (2003)
18. A. V. Prokhorov, L. M. Hanssen, Numerical Modeling of an Integrating Sphere Radiation Source, Proc. SPIE **4775**, Modeling and Characterization of Light Sources, C. Benjamin Wooley, Ed., 106-118 (2002).
19. I. Manno. Introduction to the Monte-Carlo Method. Akademiai Kiado, Budapest (1999).
20. J. Spanier and E. M. Gelbard, Monte Carlo Principles and Neutron Transport Problems, Addison-Wesley, Reading, MA (1969).
21. P. Y. Barnes, E. A. Early. Diffuse reflectance of sintered and pressed polytetrafluoroethylene (PTFE). Proc. SPIE, vol. 3426, 190-193 (1998).
22. B. T. McGuckin, D. A. Haner, R. T. Menzies. Multiangle Imaging Spectroradiometer: optical characterization of the calibration panels. Applied Optics, vol. 36, No. 27, 7016-7022 (1997).

Last Page